

Strong and broadly tunable plasmon resonances in thick films of aligned carbon nanotubes

Kuan-Chang Chiu^{1,2}, Abram L. Falk^{1,*}, Po-Hsun Ho¹, Damon B. Farmer¹, George Tulevski¹, Yi-Hsien Lee², Phaedon Avouris¹, Shu-Jen Han¹

¹IBM T. J. Watson Research Center, Yorktown Heights, New York, 10598, USA

²Dept. of Mat. Sci. and Eng., National Tsing-Hua University, Hsinchu, 30013 Taiwan

Abstract:

Low-dimensional plasmonic materials can function as high quality terahertz and infrared antennas at deep subwavelength scales. Despite these antennas' strong coupling to electromagnetic fields, there is a pressing need to further strengthen their absorption. We address this problem by fabricating thick films of aligned, uniformly sized carbon nanotubes and showing that their plasmon resonances are strong, narrow, and broadly tunable. With thicknesses ranging from 25 to 250 nm, our films exhibit peak attenuation reaching 70%, quality factors reaching 9, and electrostatically tunable peak frequencies by a factor of 2.3 \times . Excellent nanotube alignment leads to the attenuation being 99% linearly polarized along the nanotube axis. Increasing the film thickness blueshifts the plasmon resonators down to peak wavelengths as low as 1.4 μm , promoting them to a new near-infrared regime in which they can both overlap the S₁₁ nanotube exciton energy and access the technologically important infrared telecom band.

Keywords: Carbon nanotube, plasmon, resonator, nanophotonics, infrared, multispectral

Main text:

The Fabry-Pérot plasmon resonances of carbon nanotubes, longitudinal charge oscillations bound by the nanotube ends¹⁻⁶, have remarkable properties and a strong technological potential. They can concentrate light into nanoscale volumes³ and have a natural application to surface-enhanced infrared absorption (SEIRA) spectroscopy^{6,7}. Moreover, along with analogous resonances in graphene⁸⁻¹³, they are a promising basis for a new class of fast and efficient photothermoelectric photodetectors¹⁴⁻¹⁶. Tunability with length^{17,18} and free-charge density^{19,20} has allowed nanotube resonances to span wavelengths from the terahertz/far-infrared¹⁷⁻²¹ (as high as 200 μm ²¹) to the mid-infrared⁶, to even the near-infrared (down to 1.4 μm), as we show in this work. Taken together, these properties make nanotube plasmonics a

* alfalk@us.ibm.com

promising foundation for multispectral cameras that use a single photosensitive material to achieve vision through the entire infrared range.

However, in order for photodetectors comprising low-dimensional materials to be externally efficient, a key hurdle is achieving high absorption. Strategies to enhance absorption have included incorporating graphene into external antennas²² or optical cavities²³, engineering interference with substrate dielectrics²⁴, and using multilayer graphene or graphene/insulator stacks²⁵. Each has its own advantages and drawbacks. For instance, on-chip interference could lead to total light absorption²⁴ but constrains the resonator shape and substrate type. Solution-processed thick films of carbon nanotubes offer a particularly clear-cut route to high absorption. In addition, semiconducting nanotubes can be purified in solution and exhibit a higher photothermoelectric coefficient than either metallic nanotubes or graphene²⁶.

For this Letter, we assembled thick films of uniform nanotube-plasmon resonators, resulting in strong absorption and narrow ensemble linewidths. The peak attenuation that we observe (up to 70%) is markedly higher than both the ~2% peak attenuation observed in a thin film ($t = 6$ nm) of nanotube resonators⁶ and the ~6% peak attenuation typically seen in graphene nanoribbons⁹. The Q factors are as high as 9, attenuation is 99% linearly polarized, and the plasmon-resonance frequencies are electrostatically tunable by a factor of 2.3 \times , a higher factor than the 1.4 \times observed⁶ in thin nanotube films. We tune the plasmon resonators through the nanotube's S_{11} exciton to wavelengths as low as 1.4 μm , half the wavelength of previously fabricated nanotube resonators. Our results show that nanotube-plasmon resonators provide an exciting pathway toward efficient and broadband infrared cameras, compact chemical sensors, and optoelectronics at deep subwavelength scales.

To fabricate these films, we made use of a controlled vacuum filtration method²⁷ to produce thick films of remarkably well-aligned nanotubes (Fig 1(a) and Supporting Information (SI)). We dispersed semiconducting nanotubes in an aqueous solution with the surfactant sodium dodecylbenesulfonate (SDBS), sonicated and centrifuged the solution, and filtered the supernatant through polycarbonate filter membranes at a very low filtration speed (1 ml/hr). The nanotube alignment is templated by grooves in the filter paper, with the overall degree of alignment determined by the competition between van der Waals forces, pressure from vacuum pumping, and electrostatic interactions between nanotubes deriving from their surface charge.

This method is simple, low-cost, and scalable up to large areas. Over our 1-inch filters, it reliably produced uniform films of globally aligned nanotubes, with the thickness (t) ranging from a moderate 25 nm to an ultrathick 250 nm.

To unify the nanotube length, we transferred the films to high-resistivity silicon substrates (Fig. 1(b)-(c)), dissolved the filter paper that had supported them, and used electron-beam lithography and reactive ion oxygen etching to pattern the films into stripes of uniform nanotube segments, with segment length (L) ranging from 100 nm to 800 nm (Fig. 1(d)-(g)). In atmospheric conditions, water absorption naturally induces positive charge carriers in the nanotubes²⁸. We also exposed the nanotubes to either NO₂ gas or HNO₃ vapor, strong oxidizers that induce much higher free-charge densities²⁹. We used micro Fourier-transform infrared spectroscopy (μ -FTIR) to measure the films' attenuation at room temperature, with each measurement incorporating 10-100 million nanotubes in a $\sim(50 \mu\text{m})^2$ area. For films with resonant frequencies exceeding 6000 cm⁻¹, we measured attenuation in a (5 mm)² area, using an ultraviolet-visible-near-infrared (UV-VIS-NIR) spectrometer.

We observe prominent, narrow attenuation peaks (ν_p) centered at mid- and near-infrared frequencies (Fig. 2). Three key characteristics prove that these peaks indeed correspond to nanotube-plasmon resonance. First, the center frequency of the peak is a strongly decreasing function of L (Fig. 2(a)), as expected from a Fabry-Pérot resonance. Second, exposure to NO₂ gas causes the resonance to blue-shift and to intensify (Fig. 2(b)), as expected from a plasmon resonator whose free charge density is increasing. As the NO₂ desorbs over a period of several days, the plasmon attenuation shifts back to its original curve. Finally, we can separately observe both the plasmon resonance and the S₁₁ exciton peak (Fig. 2(c) and 3), verifying that the plasmon resonance peak is distinct from S₁₁. These characteristics confirm that the ν_p attenuation peaks correspond to plasmon resonance.

Thick-film-nanotube plasmon resonators are notably blueshifted from those in thin films⁶ with the same L . This shift can be understood as a coupled antenna effect^{30,31}, in which charges in a given nanotube are accelerated by the electric field deriving from plasmons in neighboring nanotubes. In one of our thickest films ($t = 220$ nm, $L = 200$ nm), the plasmon resonance frequency reaches 7000 cm⁻¹ (Fig. 3), over twice the 3000 cm⁻¹ frequency observed⁶ in a highly doped thin film of much shorter nanotubes ($t = 6$ nm and $L = 30$ nm), and a factor of 2.3 \times the

resonance frequency of the same film when undoped (Fig. 3, inset). Altogether, the ν_p frequencies that we observed ranged from 1000 cm^{-1} (Fig. S2 in SI) up to 7000 cm^{-1} , or equivalently, 1.4 to $10 \text{ }\mu\text{m}$. By reaching both the S_{11} exciton energy and the $1.55\text{-}\mu\text{m}$ telecom wavelength, nanotube plasmon resonators can now be applied to make nanophotonic and optoelectronic devices in this technologically important range.

Because nearly all applications of plasmonics are limited by dissipation, an important metric is the Q factor, which is inversely proportional to the ensemble dissipation rate. Calculating $Q = \nu_p/\Delta\nu_p$, where $\Delta\nu_p$ is the full-width-at-half-maximum of the plasmon resonance centered at ν_p , we find our films to have Q factors as high as 9.0 (inset to Fig. 2(a)). The trend of decreasing Q factor with increasing L can be understood to derive from the decrease in nanotube-length uniformity as L approaches the average nanotube length in our solution, which is $\sim 500 \text{ }\mu\text{m}$. Our Q factors are significantly higher than those previously observed in thin nanotube films⁶ ($Q \sim 3$ when not hybridized with phonons), and even higher than the $Q \sim 5$ typically seen in graphene nanoribbons⁹. These high Q factors reflect the excellent nanotube alignment that vacuum filtration produces.

Peak attenuation, another metric of our film's performance, is as high as 70% (Fig. 2(a) and Fig. S3 in SI) of the polarized incident light. Due to limitations of our lithography and etching processes, our films consist of nanotubes only covering 30-70% of the chip surface in the measurement area (see. Fig. 1(g)). This limitation is responsible for the decreasing peak attenuation with decreasing L seen in Fig. 2(a). If we were to normalize the attenuation by a geometrical factor accounting for this partial coverage, the normalized attenuation would reach $>95\%$. In the future, simply improving the verticality of the etching process ought to allow nearly total attenuation in thick nanotube films.

For films with lower frequency resonances (i.e. approaching 1000 cm^{-1}), the lineshapes are asymmetrical (Fig. 4). We fit these curves to Breit-Wigner-Fano lineshapes^{32,33}:

$$A(\nu) = I \frac{(F\gamma + \nu - \nu_0)^2}{(\nu - \nu_0)^2 + \gamma^2} \quad (1)$$

with I the intensity, ν_0 and γ the position and linewidth of the resonance, respectively, and F the Fano parameter, which characterizes the resonance's degree of asymmetry. The $A(\nu)$ fits show excellent agreement to the experimentally measured lineshapes. These Fano lineshapes can be understood as interference between the plasmons and LO phonons in the substrate⁶ (see SI for further discussion). More generally, this type of plasmon-phonon coupling indicates that thick nanotube films could be used for surface-enhanced infrared absorption (SEIRA)³⁴⁻³⁶, in which the nanotube plasmons strengthen the vibrational absorption from nearby molecules.

Excellent alignment of our nanotubes leads to the plasmon attenuation being nearly entirely polarized. To precisely determine the degree of polarization, we fit $A(\nu)$ lineshapes to Eq. 1 as a function of incident light polarization (θ) (Fig. 4). The overall degree to which the attenuation is linearly polarized, $(I_{\parallel} - I_{\perp}) / (I_{\parallel} + I_{\perp})$, with I_{\parallel} (I_{\perp}) denoting the fitted intensity parallel (perpendicular) to the axis of the nanotubes, is 99.3%. Thick nanotube films are therefore an ideal material system for infrared and terahertz polarizers³⁷, as well as metamaterials requiring an extremely asymmetric dielectric constant³⁸.

For low-dimensional materials, the general shape of the plasmon-dispersion curve is determined by geometrical considerations. As a 1D system, isolated nanotubes are expected to have an approximately linear ν vs q relationship², where the wavevector $q = \pi / L$. For graphene nanoribbons, a 2D system, $\nu \propto \sqrt{q}$.⁹ For our thick films, ν exhibits a notably sublinear dependence with both q (Fig. 5(a)) and t (Fig. 5(b),(c)). Fitting both L - and t -dependence together, we find that ν is well-fit to the function:

$$\nu_p = \nu_0 \sqrt{tq}, \quad (2)$$

with $\nu_0 = 3335 \text{ cm}^{-1}$ immediately after NO_2 exposure (Fig. 5(b),(c)). Over time, as the films' charge density decreases, ν_0 decreases by a factor of ~ 2 . While Eq. 2 is undoubtedly an approximation, it clearly indicates that in thick films, inter-nanotube coupling causes the shape of the dispersion curve to deviate from that of an isolated 1D plasmonic system. From a

technological perspective, Eq. (2) provides a means by which the resonant frequency of nanotube films can be rationally controlled.

Different types of nanotube films may find different applications. Thick and/or dense nanotube films are ideal for near-infrared detectors, since their resonant frequencies are higher, whereas thin or loosely packed nanotube films would allow analytes to intercalate into the film and be better for SEIRA. Thin films are more amenable than thick films to being tuned with an electrical gate, though interestingly, the $2.3\times$ increase in v_p that we observe with charge-transfer doping in our very thick ($t = 220$ nm) film is significantly higher than the factor of $1.4\times$ observed in $t = 6$ nm films⁶ and $t = 40$ nm films (Fig. S2 in SI). An important open question is the role of plasmon tunneling in dense nanotube films: are the plasmons' charges confined to individual nanotubes, or do they tunnel across nanotube-nanotube interfaces? A related phenomenon, the hot-carrier photothermoelectric effect¹⁶, is a promising mechanism for high-speed photodetectors in which excited charges tunnel into metal contacts.

In conclusion, we showed that thick films of uniformly sized carbon nanotubes can support coherent plasmon resonances that are highly absorptive, highly polarized, and tunable up to near-infrared telecom frequencies. The key to developing these resonators into high-performance infrared- and terahertz-frequency photodetectors will now be engineering the interface from nanotubes to metal contacts. One promising approach would be to anneal refractory metal contacts³⁹ that form an end-bonded carbide to the thick nanotube film. Nanotube-plasmon resonators could also create quasi-coherent light sources when they concentrate thermal emission or electroluminescence into their resonant frequency⁴⁰, or even plasmonic lasers¹³. Together, these detectors and light sources would make carbon nanotubes a pathway to integrated multispectral nanophotonics.

Acknowledgments: The authors thank Javier García de Abajo and Jerry Tersoff for discussions, and Jim Bucchignano for performing the electron-beam lithography.

Supporting Information: Detailed procedure for fabricating thick films of aligned carbon nanotubes, spectroscopy methods, supporting discussion of background subtraction and Q factor calculation, and supporting figures portraying plasmon attenuation in thinner nanotube films.

Conflict of interest disclosure: The authors declare no competing financial interest.

References:

- (1) Slepyan, G. Y.; Maksimenko, S. A.; Lakhtakia, A.; Yevtushenko, O.; Gusakov, A. V. *Phys. Rev. B* **1999**, *60* (24), 17136–17149.
- (2) Nakanishi, T.; Ando, T. *J. Phys. Soc. Japan* **2009**, *78* (11), 114708.
- (3) Shi, Z.; Hong, X.; Bechtel, H. A.; Zeng, B.; Martin, M. C.; Watanabe, K.; Taniguchi, T.; Shen, Y.-R.; Wang, F. *Nat. Photonics* **2015**, *9* (8), 515–519.
- (4) Soto Lamata, I.; Alonso-Gonzalez, P.; Hillenbrand, R.; Nikitin, A. Y. *ACS Photonics* **2015**, *2* (2), 280–286.
- (5) Martin-Moreno, L.; De Abajo, F. J. G.; Garcia-Vidal, F. J. *Phys. Rev. Lett.* **2015**, *115*, 173601.
- (6) Falk, A. L.; Chiu, K.; Farmer, D. B.; Cao, Q.; Tersoff, J.; Lee, Y.-H.; Avouris, P.; Han, S. *Phys. Rev. Lett.* **2017**, *257401* (25), 1–6.
- (7) De Vega, S.; Cox, J. D.; De Abajo, F. J. G. *Phys. Rev. B* **2016**, *94* (7), 1–6.
- (8) Koppens, F. H. L.; Chang, D. E.; García de Abajo, F. J.; Abajo, F. J. G. *Nano. Lett.* **2011**, *11* (8), 3370–3377.
- (9) Yan, H.; Low, T.; Zhu, W.; Wu, Y.; Freitag, M.; Li, X.; Guinea, F.; Avouris, P.; Xia, F. *Nat. Photonics* **2013**, *7* (5), 394–399.
- (10) Yan, H.; Low, T.; Guinea, F.; Xia, F.; Avouris, P. *Nano Lett.* **2014**, *14* (8), 4581–4586.
- (11) Ju, L.; Geng, B.; Horng, J.; Girit, C.; Martin, M.; Hao, Z.; Bechtel, H. a; Liang, X.; Zettl, A.; Shen, Y. R.; Wang, F. *Nat. Nanotechnol.* **2011**, *6* (10), 630–634.
- (12) Koppens, F.; Lundberg, M. B.; Polini, M.; Low, T.; Avouris, P. In *2D Materials: Properties and Devices*; Cambridge University Press, 2017.
- (13) Rana, F. *Conf. Proc. - Lasers Electro-Optics Soc. Annu. Meet.* **2007**, *7* (1), 862–863.
- (14) He, X.; Fujimura, N.; Lloyd, J. M.; Erickson, K. J.; Talin, a A.; Zhang, Q.; Gao, W.; Jiang, Q.; Kawano, Y.; Hauge, R. H.; Léonard, F.; Kono, J. *Nano Lett.* **2014**, *14* (7), 3953–3958.
- (15) He, X.; Léonard, F.; Kono, J. *Adv. Opt. Mater.* **2015**, *3* (8), 989–1011.
- (16) Cai, X.; Sushkov, A. B.; Suess, R. J.; Jadidi, M. M.; Jenkins, G. S.; Nyakiti, L. O.; Myers-Ward, R. L.; Li, S.; Yan, J.; Gaskill, D. K.; Murphy, T. E.; Drew, H. D.; Fuhrer, M. S. *Nat. Nanotechnol.* **2014**, *9* (10), 814–819.
- (17) Shuba, M. V.; Paddubskaya, a. G.; Plyushch, A. O.; Kuzhir, P. P.; Slepyan, G. Y.; Maksimenko, S. A.; Ksenevich, V. K.; Buka, P.; Seliuta, D.; Kasalynas, I.; Macutkevicius, J.;

- Valusis, G.; Thomsen, C.; Lakhtakia, a. *Phys. Rev. B* **2012**, *85* (16), 14–17.
- (18) Morimoto, T.; Joung, S.-K.; Saito, T.; Futaba, D. N.; Hata, K.; Okazaki, T. *ACS Nano* **2014**, *8* (10), 9897–9904.
- (19) Akima, N.; Iwasa, Y.; Brown, S.; Barbour, A. M.; Cao, J.; Musfeldt, J. L.; Matsui, H.; Toyota, N.; Shiraishi, M.; Shimoda, H.; Zhou, O. *Adv. Mater.* **2006**, *18* (9), 1166–1169.
- (20) Zhang, Q.; Haroz, E. H.; Jin, Z.; Ren, L.; Wang, X.; Arvidson, R. S.; Luttge, A.; Kono, J. *Nano Lett.* **2013**, *13* (12), 5991–5996.
- (21) Bommeli, F.; Degiorgi, L.; Wachter, P.; Bacsá, W. S.; De Heer, W. A.; Forro, L. *Solid State Commun.* **1996**, *99* (7), 513–517.
- (22) Vicarelli, L.; Vitiello, M. S.; Coquillat, D.; Lombardo, A.; Ferrari, a. C.; Knap, W.; Polini, M.; Pellegrini, V.; Tredicucci, A. *Nat. Mater.* **2012**, *11* (10), 865–871.
- (23) Furchi, M.; Urich, A.; Pospischil, A.; Lilley, G.; Unterrainer, K.; Detz, H.; Klang, P.; Andrews, A. M.; Schrenk, W.; Strasser, G.; Mueller, T. *Nano Lett.* **2012**, *12* (6), 2773–2777.
- (24) Thongrattanasiri, S.; Koppens, F. H. L.; Garcia De Abajo, F. J. *Phys. Rev. Lett.* **2012**, *108* (4), 1–5.
- (25) Yan, H.; Li, X.; Chandra, B.; Tulevski, G.; Wu, Y.; Freitag, M.; Zhu, W.; Avouris, P.; Xia, F. *Nat. Nano.* **2012**, *7* (5), 330–334.
- (26) Erikson, K. J.; He, X.; Talin, A. A.; Mills, B.; Hauge, R. H.; Iguchi, T.; Fujimura, N.; Kawano, Y.; Kono, J.; Léonard, F. *ACS Nano* **2015**, *9* (12), 11618–11627.
- (27) He, X.; Gao, W.; Xie, L.; Zhang, Q.; Lei, S.; Li, B.; Robinson, J. M.; Doorn, S. K.; Vajtai, R.; Ajayan, P. M.; Adams, W. W. *Nat. Nano.* **2016**, *11* (April), 1–21.
- (28) Kim, W.; Javey, A.; Vermesh, O.; Wang, Q.; Li, Y.; Dai, H. *Nano Lett.* **2003**, *3* (2), 193–198.
- (29) Kong, J.; Franklin, N. R.; Zhou, C.; Chapline, M. G.; Peng, S.; Cho, K.; Dai, H. *Science* (80-.). **2000**, *287*, 622–625.
- (30) Hao, J.; Hanson, G. W. *Phys. Rev. B* **2006**, *74* (3), 1–6.
- (31) Nene, P.; Strait, J. H.; Chan, W. M.; Manolatu, C.; Tiwari, S.; McEuen, P. L.; Rana, F. *Appl. Phys. Lett.* **2014**, *105* (14).
- (32) Fano, U. *Phys. Rev.* **1961**, *124* (6), 1866–1878.
- (33) Luk'yanchuk, B.; Zheludev, N. I.; Maier, S. a; Halas, N. J.; Nordlander, P.; Giessen, H.; Chong, C. T. *Nat. Mater.* **2010**, *9* (9), 707–715.
- (34) Hartstein, A.; Kirtley, J. R.; Tsang, J. C. *Phys. Rev. Lett.* **1980**, *45* (3), 201–204.
- (35) Farmer, D. B.; Avouris, P.; Li, Y.; Heinz, T. F.; Han, S. *ACS Photonics* **2016**, *3*, 553–557.
- (36) Le, F.; Brandl, D. W.; Urzhumov, Y. A.; Wang, H.; Kundu, J.; Halas, N. J.; Aizpurua, J.;

- Nordlander, P. *ACS Nano* **2008**, 2 (4), 707–718.
- (37) Ren, L.; Pint, C. L.; Booshehri, L. G.; Rice, W. D.; Wang, X.; Hilton, D. J.; Takeya, K.; Kawayama, I.; Tonouchi, M.; Hauge, R. H.; Kono, J. *Nano Lett.* **2009**, 9 (7), 2610–2613.
- (38) Iorsh, I. V.; Mukhin, I. S.; Shadrivov, I. V.; Belov, P. A.; Kivshar, Y. S. *Phys. Rev. B* **2013**, 87 (7).
- (39) Cao, Q.; Han, S.-J.; Tersoff, J.; Franklin, A. D.; Zhu, Y.; Zhang, Z.; Tulevski, G. S.; Tang, J.; Haensch, W. *Science* (80-.). **2015**, 350 (6256), 68–72.
- (40) Liu, J.; Guler, U.; Lagutchev, A.; Kildishev, A.; Malis, O.; Boltasseva, A.; Shalaev, V. M. *Opt. Mater. Express* **2015**, 5 (12), 2721.

Figures

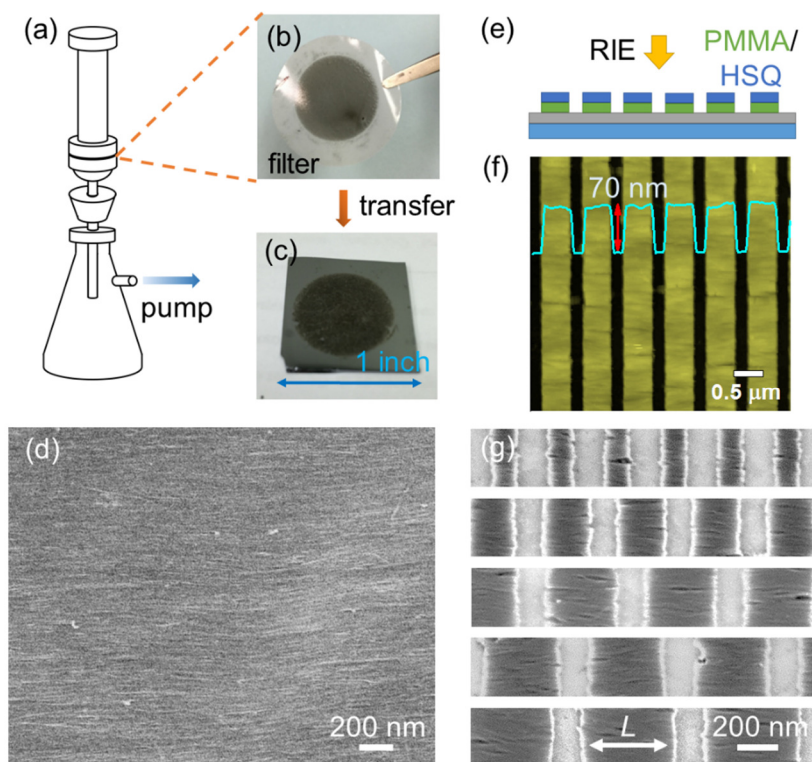


Figure 1. Preparation of thick films of aligned, uniformly sized carbon nanotubes. (a) Slow vacuum filtration produces (b) thick films of aligned carbon nanotubes on filter paper. (c) The nanotube films are transferred to silicon and exhibit (d) global alignment across the 1” circle in scanning electron microscopy (SEM). (e) The nanotubes are cut into stripes by reactive ion etching (RIE) through a poly(methyl methacrylate) / hydrogen silsesquioxane (PMMA/HSQ) mask, which was patterned with electron beam lithography. (f) Atomic force microscopy shows film thickness (t) to range from 25 to 250 nm. (g) SEM image of cut, aligned thick films of nanotubes.

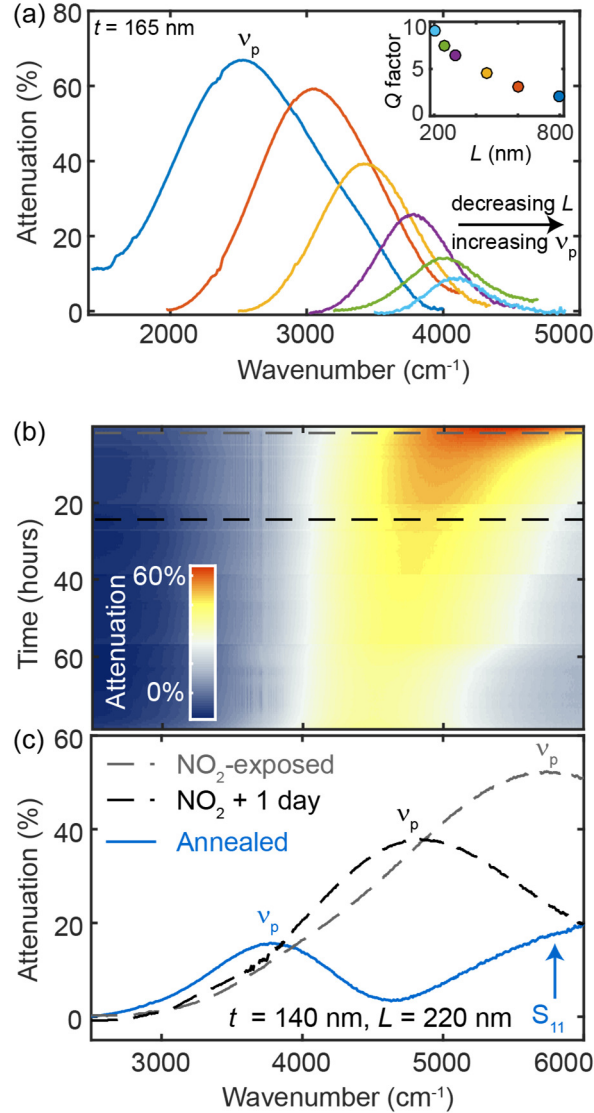


Figure 2. Attenuation from thick-film nanotube plasmon resonators as a function of L and doping level. (a) Attenuation as a function of L , with t fixed to 165 nm and the nanotubes not intentionally doped. The attenuation is measured in a μ -FTIR apparatus with the light source polarized along the nanotube axis. From left to right, $L = 800$ nm, 600 nm, 450 nm, 300 nm, 250 nm, and 200 nm. Inset: Q factors as a function of L , reaching $Q = 9.0$ at $L = 200$ nm. The circles are color-coded to match the curves in the main panel. (b) Attenuation of a $t = 140$ nm, $L = 220$ nm film as a function of time after NO_2 exposure, which is a proxy for the doping level. The dashed lines represent line cuts plotted in (c). (c) Attenuation immediately after NO_2 exposure (maximum doping level), 1 day after NO_2 exposure (intermediate doping level). The solid blue line is the attenuation when the film has been annealed at 550 °C (minimal doping).

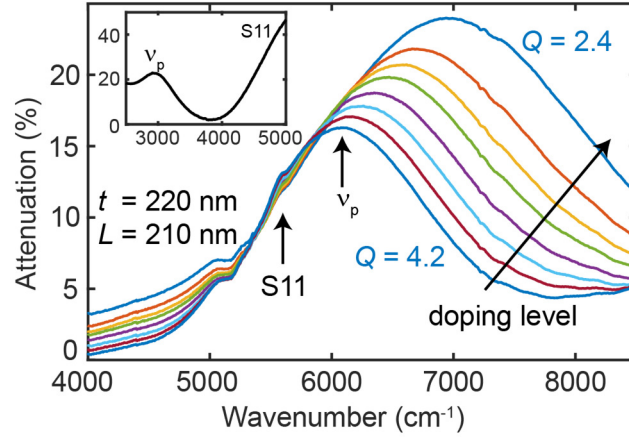


Figure 3. High-frequency (near-infrared) plasmon resonance of a thick ($t = 220$ nm) nanotube film at 8 different doping levels, measured in a UV-VIS-NIR spectrometer with an unpolarized light source. The curves represent time after exposure to HNO_3 vapor, with 10 minute intervals between curves, starting immediately after HNO_3 exposure. The v_p peak can exceed the S_{11} energy and be as high as 7000 cm^{-1} ($1.43\text{ }\mu\text{m}$). Inset: Attenuation vs. wavenumber when the film is annealed (minimal doping).

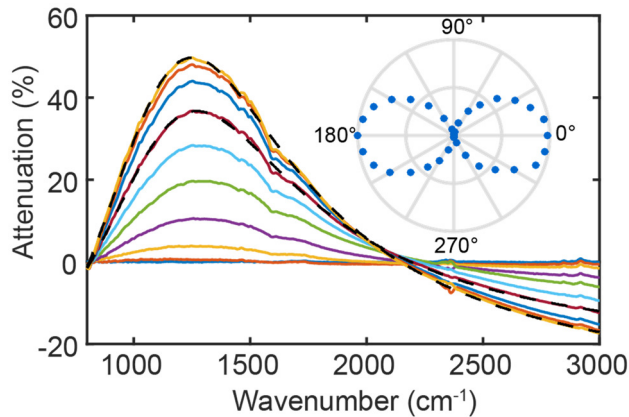


Figure 4. Plasmon resonance as a function of incident light polarization, with θ representing deviation from the nanotube alignment axis, taken at 10° intervals. A background curve representing is subtracted from all curves equally (see SI). The attenuation curves have excellent fits to Fano functions (black dashed lines, plotted for $\theta = 0^\circ$ and $\theta = 30^\circ$). Inset: $I(\theta)$, fitted from the polarization-dependent attenuation using Eq. (1). The attenuation is fit to be 99% polarized along the axis of the nanotubes.

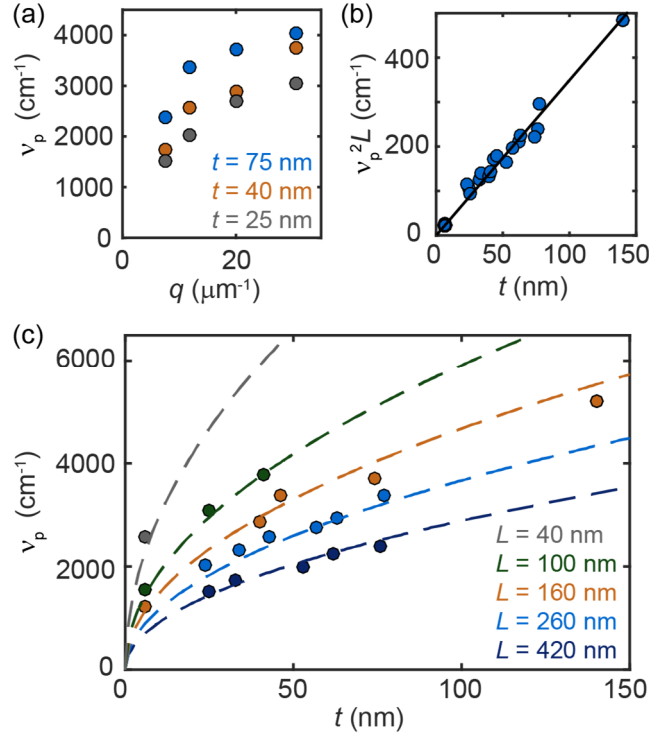


Figure 5. Evolution of v_p with q ($= \pi/L$) and t . (a) v_p has a sublinear dependence on q . (b) When both L and t are varied, $v_p^2 L$ has a linear relationship with t , indicating that v_p has a good fit to Eq. 2. (c) v_p , plotted as a function of t . The fit (dashed lines) to Eq. 2 is a global fit to the data from all five curves, yielding $v_0 = 3335$ cm⁻¹. The three $t = 6$ nm data points are appropriated from Ref. 6. All the data in this figure are with highly doped nanotubes, measured immediately after NO₂ gas exposure.

Supporting Information for

Strong and broadly tunable plasmon resonances in thick films of aligned carbon nanotubes

Kuan-Chang Chiu^{1,2}, Abram L. Falk¹, Po-Hsun Ho¹, Damon B. Farmer¹, George Tulevski¹, Yi-Hsien Lee², Phaedon Avouris¹, Shu-Jen Han¹

¹IBM T. J. Watson Research Center, Yorktown Heights, New York, 10598, USA

²Dept. of Mat. Sci. and Eng., National Tsing-Hua University, Hsinchu, 30013 Taiwan

Contents

1. Detailed procedure for fabricating thick films of aligned carbon nanotubes.
2. Spectroscopy methods
3. Discussion of background subtraction and Q factor calculation
4. Lower-frequency plasmon resonances in thinner films
5. Additional L -dependent series of plasmon resonances

1. Detailed procedure for fabricating thick films of aligned carbon nanotubes.

A vacuum filtration method was used to assemble the thick nanotube films²⁵. For the experimental setup (Fig. 1(a) of main text), the key components are a 15 mL glass funnel and a fritted glass filter support with a silicone stopper (Millipore® XX1002500 glass microanalysis), both purchased from Fisher Scientific Company. The vacuum filtration method consists of four steps:

1. Dispersing the carbon nanotubes in a surfactant solution.
2. Vacuum-filtering the nanotube dispersion onto a filtration membrane.
3. Transferring the CNT film onto a target substrate.
4. Dissolving the membrane in a solvent.

An arc-discharge single-walled carbon nanotube powder with an average diameter of 1.4 nm and semiconducting purity of > 90% (P2-SWCNT, Carbon Solution) was dispersed in aqueous solution with sodium dodecylbenesulfonate (SDBS, Sigma-Aldrich) as a surfactant. The starting concentration was 0.4 mg/ml for nanotubes and 0.4% (wt/vol) for SDBS. The nanotube powder and surfactant was first dispersed by bath sonication for 15 minutes and then further sonicated with

a tip sonicator for 45 min. Pulse sonication used a 3 sec/1 sec on/off duty cycle, and a circulating cooling water bath during to prevent heating of the dispersion. Next, the suspension was centrifuged for 1 hour at 38,000 r.p.m to remove large bundles from the suspension. The supernatant was extracted and then diluted to a final SDBS concentration of 0.08%.

The well-dispersed solution was filtered with polycarbonate filter membranes (Whatman Nuclepore track-etched polycarbonate hydrophilic membranes, 0.05 μm pore size) at a very low filtration speed of ~ 1 ml/hr. The filter membrane is treated with O_2 plasma for 30 seconds prior to deposition. The reduced filtration speed could be controlled by adjusting a needle valve and monitoring pressure with a differential vacuum pressure gauge.

The silicon substrates onto which we transferred the nanotube films consist of high-resistivity silicon with 10-nm of HfO_2 , which was deposited by atomic layer deposition. For transferring the nanotube film, a droplet of water was placed on the target substrate. The as-deposited films on membranes were then attached on the target substrates with the side of nanotube film touching the substrate surface. A glass slide was used to cover the whole membrane with a small amount of pressure to make the film stick to the surface of the substrate firmly. Nitrogen gas was then used to dry the substrate.

To remove the membrane, the whole substrate was immersed into an organic solvent (N-methyl-2-pyrrolidone or chloroform) to dissolve the membranes. The samples were then annealed under a vacuum of 10^{-7} Torr at 500 degrees for thirty minutes to burn off any remaining organic residue.

2. Spectroscopy methods

The attenuation spectra were measured in a Bruker Nicolet 8700 μ -FTIR system. The diameter of the focused beam size is 25 μm , and each measurement was integrated for a 30-second period. Before each spectrum is taken, a background spectrum is taken, on an area of the chip in which the carbon nanotubes have been completely etched away. The spectrometer outputs absorbance relative to the background spectrum. We then calculate the attenuation ($A(\nu)$) as

$$A(\nu) = 1 - 10^{-\text{absorbance}(\nu)} \quad (\text{S1})$$

To measure the high frequency plasmon resonances in thick films ($\nu_p > 6000 \text{ cm}^{-1}$, see Fig. 3 of main text), which were out of the range of our FTIR system, we used a PerkinElmer Lambda 950 UV-VIS-NIR spectrometer. The films we prepared for use in this system were similar to the ones that we prepared for FTIR, except 1) Larger patterns ($5 \text{ mm} \times 5 \text{ mm}$) were prepared, to accommodate the larger beam size of this spectrometer, and 2) glass substrates were used instead of silicon, to reduce the substrate absorption in this higher energy regime.

3. Background subtraction and Q factor calculation

As mentioned above, all of the measurements in this paper were taken relative to a background spectrum, where the background consisted of a region of the substrate with nanotubes that have been etched away. Nonetheless, in some cases, features that we do not attribute to the plasmon resonance of the etched nanotubes remain in our spectra. For instance, S_{11} absorption can clearly be seen in Fig. 2(c) and in Fig. 3.

When calculating Q factors in this manuscript, we always calculate full-width half-max (FWHM) relative to only the shape of the plasmon resonance (ν_p). That is, we subtract off any spectral features that are not part of ν_p , and calculate the FWHM relative to the base of only the ν_p peak. Likewise, when quoting peak attenuation value, we quote the peak height of ν_p after subtracting off any non- ν_p attenuation features.

For the spectra plotted in Fig. 2(a), a constant background is subtracted from each curve to make the minimum attenuation line up with 0%. This procedure eliminates any potential contribution from S_{11} attenuation and unetched nanotubes to the peak attenuation. The spectra plotted in Figs. 2(b-c) and 3 are likewise plotted as measured, except for the subtraction of a small (2%-5%) constant attenuation.

In Fig. 4, the polarization sensitive data reveal the rising edge of a low energy peak (Fig. S1(a)). This rising edge likely corresponds to the plasmon resonance of unetched nanotubes, possibly etch-resistant nanotube bundles. We fit these data to a sum of two Fano functions, with the model that the higher energy one would correspond to the etched nanotubes (ν_p) and the

lower energy one would correspond to the unetched nanotubes. We find this lower energy rising edge to be well fit to the Fano function (Eq. 1), with parameters $\nu_0 = 960 \text{ cm}^{-1}$, $F = 0.4$, and $\gamma = 3000 \text{ cm}^{-1}$ (dashed black line in Fig. S1(a)). After subtracting this curve from all of the polarization-dependent data (Fig. S1(b)), we then refit the data to a single Fano function, with excellent fitting results (Fig. 4 in main text).

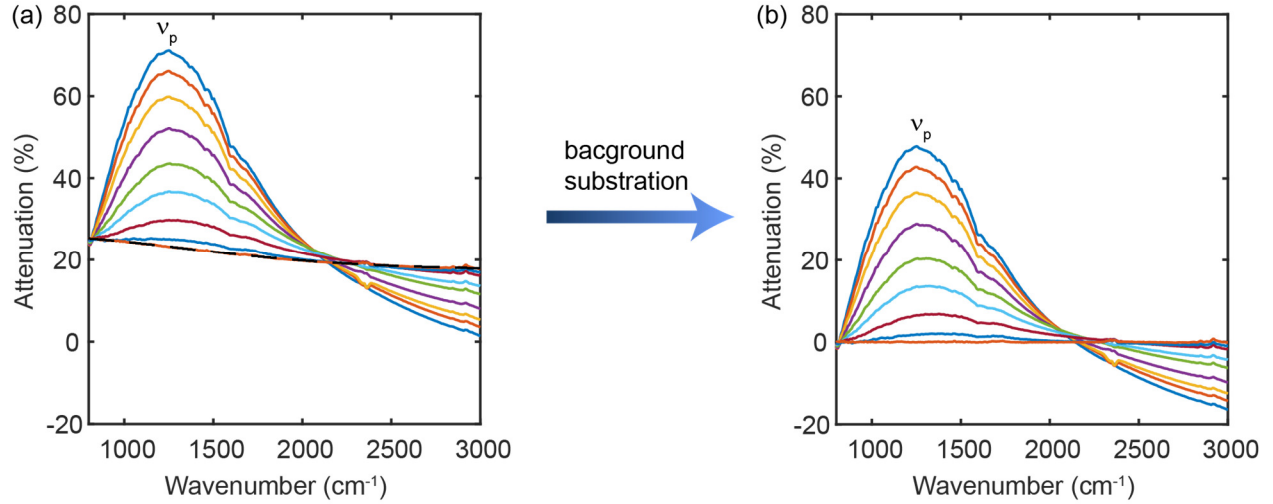


Figure S1. Background subtraction for polarization dependent data. (a) Attenuations as a function of incident light polarization, with θ representing deviation from the nanotube alignment axis, taken at 10° intervals. The dashed black curve is the fit to Eq. 1 of the rising edge of the low energy feature (fit to a peak wavenumber of 960 cm^{-1}). (b) Polarization-dependent attenuation after subtracting off the background curve. These are the curves displayed in Fig. 4 of the main text.

4. Lower-frequency plasmon resonances in thinner films

As discussed in the main text, ν_p is lower for thinner films. In a relatively thin $t = 40 \text{ nm}$ film, ν_p ranged from approximately 1000 cm^{-1} up to 3800 cm^{-1} (Fig. S2). When $\nu_p > 2000 \text{ cm}^{-1}$, the lineshapes are approximately symmetrical. However, when $\nu_p < 2000 \text{ cm}^{-1}$, the lineshapes become asymmetrical, and a sharp secondary peak at 760 cm^{-1} strengthens (marked “LO” in Fig. S2).

In previous work that studied plasmons in thin nanotube films⁶, a very similar phenomenon was observed, and the asymmetric lineshapes and secondary peak were understood to result from

plasmon-coupled longitudinal phonons in the SiO₂ substrate. In this work, we have a HfO₂ substrate, not an SiO₂ one, but the lineshapes can be understood as deriving from an analogous plasmon-coupled longitudinal optical (LO) phonon in the HfO₂ substrate.

When measured immediately after heavy p-type doping through HNO₃ vapor, the ν_p resonances are approximately 1.5 \times higher than comparable resonances in the nominally undoped nanotube film. Interestingly, this 1.5 \times factor is approximately the same as the factor observed in thin ($t = 6$ nm) nanotube films⁶ and significantly less than the 2.3 \times factor we observe for the thick nanotube films (Fig. 3 in main text). It suggests that inter-nanotube coupling is a function of doping level, thereby shifting ν_p in a thick film even more than ν_p in an isolated nanotube or thinner film would shift under a similar doping-level differential.

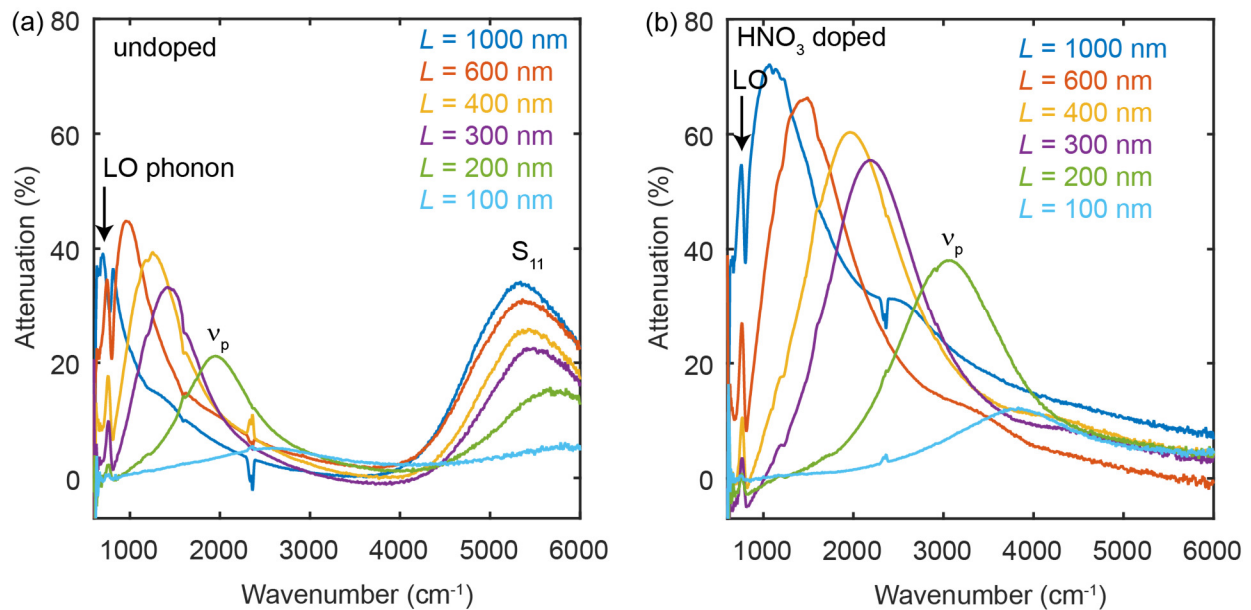


Figure S2. Lower frequency plasmon resonances on a thinner ($t = 40$ nm) carbon-nanotube film. (a) Attenuation spectra as a function of L when the nanotubes are undoped. (b) Attenuation spectra as a function of L when the films are doped with HNO₃ vapor.

5. Additional L -dependent series of plasmon resonances

As a complement to Fig 2(a), Fig. S3 presents a similar series of length-dependent plasmon resonances.

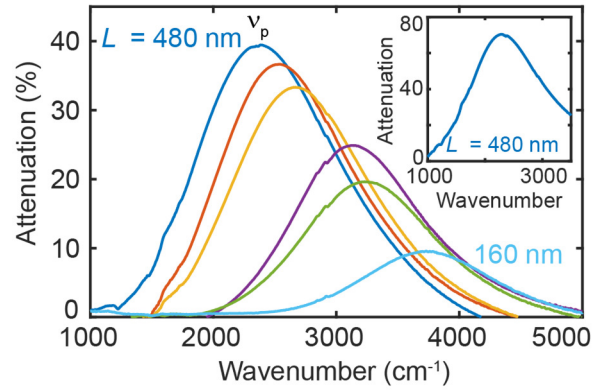


Figure S3. Attenuation as a function of L , with t fixed to 70 nm and the nanotubes in a highly doped state immediately following NO_2 exposure. The attenuation is measured in a μ -FTIR apparatus with an unpolarized light source. From left to right, $L = 480$ nm, 410 nm, 350 nm, 260 nm, 230 nm, and 160 nm, with corresponding Q factors of 1.8, 2.0, 2.1, 2.6, 2.6, and 3.0. Inset: Attenuation when incident light is polarized along the nanotube axis, reaching 70% peak attenuation.